Editors' Suggestion | Featured in Physics

First Measurement of Z Opacity Sample Evolution near Solar Interior Conditions Using Time-Resolved Spectroscopy

G. P. Loisel,[1] J. E. Bailey,[1] T. Nagayama,[1] S. B. Hansen,[1] G. S. Dunham,[1] P. D. Gard,[1] A. P. Colombo,[1] A. D. Edens,[1] R. Speas,[1] Q. Looker,[1] M. Kimmel,[1] J. L. Porter,[1] E. C. Harding,[1] G. A. Rochau,[1] C. J. Fontes,[2] J. P. Colgan,[2] C. Blancard,[3,4] Ph. Cossé,[3,4] G. Faussurier,[3,4] F. Gilleron,[3,4] J.-Ch. Pain,[3,4] and D. Aberg[5]

[1]*Sandia National Laboratories, Albuquerque, New Mexico 87185, USA*
[2]*Los Alamos National Laboratory, Los Alamos, New Mexico 87545, USA*
[3]*CEA, DAM, DIF, F-91297 Arpajon, France*
[4]*Université Paris-Saclay, CEA, LMCE, F-91680 Bruyères-le-Châtel, France*
[5]*Lawrence Livermore National Laboratory, Livermore, California 94550, USA*

(Received 30 October 2024; accepted 8 January 2025; published 3 March 2025)

Opacity model differences with Fe opacity measurements at high temperature (T > 180 eV) and high electron density ($n_e > 3 \times 10^{22}$ cm^{-3}) at nearly solar interior conditions have remained unresolved [Bailey *et al.*, Nature **517**, 56 (2015) and Nagayama *et al.*, Phys. Rev. Lett. **122**, 235001 (2019)]. Systematic errors from temporal gradients are one hypothesis for the discrepancy. Past data recorded on x-ray film provided spectral measurements over a time determined by the 2.8-ns backlighter duration. Here, we present the first measurements of opacity sample temporal evolution using novel hCMOS ultrafast x-ray camera technology. The measured conditions, measured backlighter time history, and modeled opacities are used to show that temporal gradients do not resolve the model-data discrepancy. The methods demonstrated provide potential advantages, including opacities at more extreme conditions, spectral line shift measurements, and improved measurements at other facilities.

DOI: 10.1103/PhysRevLett.134.095101

Opacity quantifies photon absorption in matter, and spectrally resolved measurements of iron opacity at temperatures >180 eV and electron densities $>3 \times 10^{22}$ cm^{-3} revealed 30%–400% model-data opacity discrepancies [1]. These conditions are similar to those at the solar convection zone base and the measurements imply the true iron opacity for solar matter is higher than models predict. While this helps resolve the long-standing puzzle [2] of standard solar models, although it has been a stimulating source of theoretical progress in the field, the discrepancy largely remains.

Hypotheses for the source(s) of the discrepancies are roughly grouped into two categories: (1) undetected flaws in the high temperature and density experiments are present and/or (2) photon absorption in high energy density matter differs from what was previously believed. Both modeling and measuring opacity are challenging at high energy density conditions, and neither possibility can be ruled out until experiment and theory are reconciled.

The Z experiments infer opacity by heating a thin sample with an x-ray source at the facility. The spectrally resolved transmission is measured with spectrometers that view the pinch-stagnation backlighter through the iron sample. All published Z opacity data used spectrometers equipped with film detectors that integrated the signal over the 2.8-ns full-width-half-maximum (FWHM) backlighter. Time-resolved data were not originally available, raising a concern that some dynamical aspects of the Z opacity platform might not be sufficiently understood. This Letter describes our first-of-its-kind tests of the time-dependent effects on Z opacity measurements using a novel time-gated detector.

First, the time-resolved measurements can expand our understanding of experiments based on 1D radiation-hydrodynamics simulations [3]. Calibrated simulations with a single scaling factor for the x-ray source intensity have reproduced measured sample conditions for all experiments at anchor 1 ($T_e \sim 156$ eV, $n_e \sim 7 \times 10^{21}$ cm^{-3}) and anchor 2 ($T_e \sim 180$–190 eV, $n_e \sim 3$–4×10^{22} cm^{-3}). The simulations predict that, during the backlighter duration, T_e and n_e drop by 14% and 70%, respectively. Comparing the opacity with and without the predicted temporal gradient effect showed that accounting for simulated temporal gradients would not resolve the model-data discrepancy [4]. However, these calibrated simulations have a few significant limitations and thus a persistent concern exists: what if the predicted sample temperature and density evolution were wrong? Here, we have reinvestigated the temporal gradient effect on Fe opacity measurements.

Second, these time-resolved measurements constrain the importance of various opacity theory revisions. For instance, More *et al.* [5] raised two-photon absorption as a potential source of discrepancy, but the importance of this process has been controversial [6]. Time-resolved

measurements could help because the magnitude of multiphoton absorption depends on the source radiance, and that radiance varies with time. Finally, if the sample conditions change with time, time-resolved measurements could help us better understand how the opacity is affected by temperature or density effects, such as populations, spectral line shapes, and continuum lowering.

In this Letter, we present the first opacity measurements of the temporal evolution of iron samples at anchor 2 conditions. The apparatus and the requirements to measure $T_e(t)$ and $n_e(t)$ from Mg K-shell tracer spectra are described. We determine the impact on past film-based measurements by using measured time-resolved temperatures, densities, and backlighter spectra and by simulating the film data formation in detail for several different opacity models. In the past, we found that the backlighter is intense over a short enough duration that the film-integrated opacity agreed with the opacity calculated at a single temperature and density [1], ruling out time-dependent effects as a source of the discrepancy. However, we also find that both the temperature and density increase over the backlight duration, in disagreement with simulations. These results strengthen our understanding, predictive capability, and the ability to design experiments at even more extreme conditions.

Time-resolved requirements and measurements—The Fe opacity sample conditions are diagnosed using absorption lines from Mg dopant comixed with the sample [7]. The Mg line optical depth spectra are fitted to infer temperature, density, and areal density. The line fits minimize χ^2, $\sum_i (\text{data}_i - \text{model}_i)^2/\text{uncertainty}_i^2$, where i corresponds to each sampled photon energy, using the Sandia-developed Dakota optimization software [8]. One challenge is that simultaneous line fitting often underestimates parameter uncertainties. To avoid this common flaw, we employ sequential line analysis that was recently developed [9]. This method provides unbiased, more realistic uncertainties, as described below. Additionally, the line fits also use novel line shape calculations using less approximations than previous calculations [10].

Any residual background that might affect line depths is measured and accounted for [11] by comparing the optically thick Heα and Heβ line center transmissions with model predictions [12]. The high optical depth makes the results very insensitive to the spectral synthesis model. We infer the electron density and sample areal density by individually fitting Heβ, Heγ, Heδ, and Lyβ. The densities we infer from these lines are typically not identical due to imperfections in both the line-shape models and experimental measurements, data reduction, and analysis assumptions. Hence, we average the results. We infer the electron temperature by individually fitting all possible line pairs with lines coming from two adjacent charge states using Lyα, Lyβ, Heβ, Heγ, Heδ, He-like satellites to Lyα, and Li-like satellites to Heβ. As with the density, the results from different line ratios are typically not identical and an average is used for the final result.

The parameter uncertainties are dependent on multiple contributions. A 25% background uncertainty is estimated from the standard deviation of the Heα and Heβ background inferences. The density and temperature fits are repeated using the nominal, upper bound, and lower bound for the background to propagate the background uncertainty. The fit quality depends on the measurement signal-to-noise (S/N) ratio. S/N varies over time and is lower at early and late times since the backlighter radiance can be as low as 1% of the peak value (beyond ± 3 ns from $t = 0$ defined as the peak of the backlighter). The limited S/N mainly affects the weakest lines, e.g., Lyβ or Heδ. The uncertainties thus comprise the background uncertainties, fit uncertainty from the line optical depth statistics, and line-to-line variations. Using multiple lines helps alleviate and account for the model uncertainties (also see [13]). The temperature uncertainty also includes the contribution that arises from the modest density sensitivity of the line ratios; thus, the density uncertainty must be propagated into the temperature uncertainty.

The spectrometers are the same [14] as in our past published data except for some of the detectors. Six spectrometers are fielded on each experiment. Two spectrometers are coupled to the hCMOS ultrafast x-ray imagers (UXI) [15–19] that were developed at Sandia National Laboratories, instead of coupled to x-ray films. This improvement provides simultaneous film and UXI data recordings during every experiment. The UXI camera [Fig. 1(a)] uses a 12.8×25.6 mm^2 sensor with 25-μm pixels [Fig. 1(b)]. Each pixel can record four frames of 1.86-ns duration (i.e., a *single line-of-sight* recording [15]). The sensor is split into regions A and B. Since each region can record four frames, a total of eight frames can be recorded per experiment [Fig. 1(c)]. An array of two 100-μm-wide slits projects the space-resolved images with 1.1 magnification onto the two regions. A 4-inch-radius convex potassium acid phthalate crystal provides the dispersion. The detector protection is provided by the 4.1-m source-to-crystal distance, by an array of baffles, and by two layers of 0.2-μm-thick aluminized polyimide.

The UXI-based data have novel advantages, especially for absorption spectral analysis. The camera is designed for single-photon counting, thereby providing high sensitivity (e.g., higher than that of the time-integrating film). The channel crosstalk is low because the signal arises from electron-hole pairs generated directly in silicon, without the electron amplification and transport stages typically used in microchannel plate devices. This is a key advantage for recording absorption spectra that prevents bright continuum emission from artificially filling in narrow absorption lines. Furthermore, each pixel is read out multiple times in each experiment, implying perfect spatial and spectral registration between the different times, which can foster unprecedented accuracy for spectral-line-shift measurements. Also, the characterized [16,17] response is linear to better

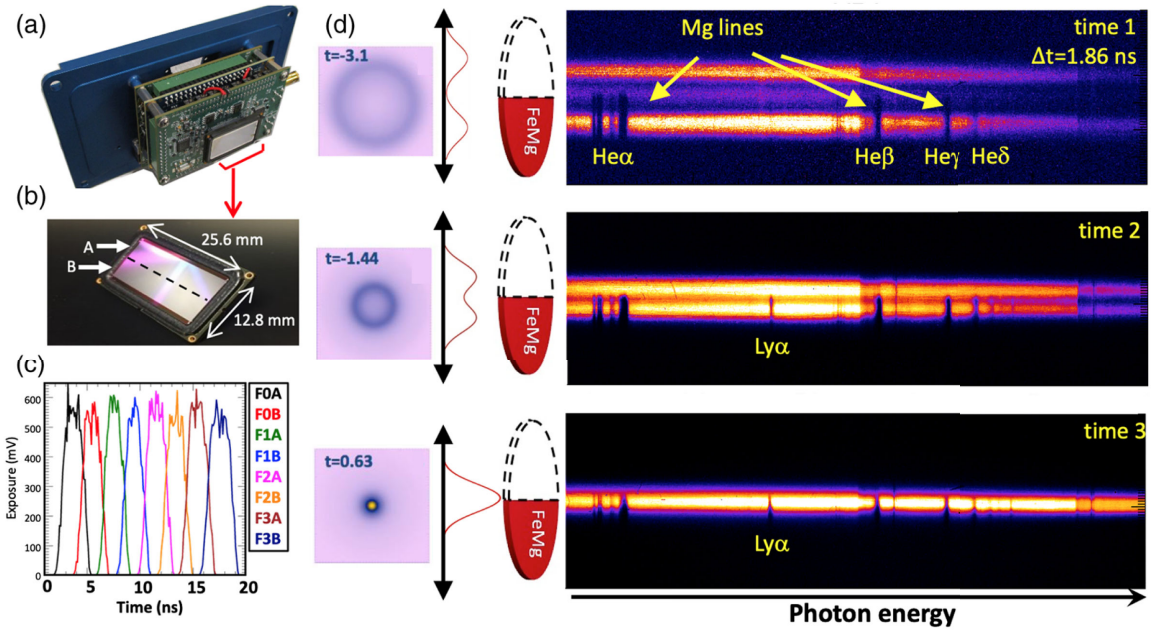

FIG. 1. (a) hCMOS UXI sensor and electronics. (b) Close-up photo of sensor. The two sensor halves (regions A and (B) designate the areas that are triggered independently from each other. (c) Gate profiles measured using a short-pulse laser can be approximated by a Gaussian profile with ∼1.86 ns FWHM. Camera region A is set to be on for 2 ns and then on for 2 ns in region B such that there is no data collection gap. Up to eight frames are possible for a total recording duration of about 16 ns with F0A, F0B, F1A, F1B, F2A, F2B, F3A, and F3B sequence. (d) Example dataset showing three images from z3365 with clear Mg absorption lines shown. A cartoon of the half-moon of the FeMg sample is on the left. Mg lines appear in the bottom half of images with 1D slit-imaging spectrometers [14]. The previously measured [20] 2D pinhole images and adjacent lineouts show the x-ray source spatial distribution as it implodes.

than 3%, ensuring accurate line-shape and line-depth measurements. Overall spectral resolution, including the camera point-spread function, is $\lambda/\delta\lambda \sim 1100$–$1200$ in the 7–9 Å Mg line range. The spatial uniformity is measured to be better than 2% [18], which is useful for the accurate interpretation of backlighter spectral shapes.

Sample evolution results of FeMg near anchor 2 conditions—We fielded UXI spectrometers for anchor 2 experiments with $T_e = 189 \pm 7$ eV, $n_e = 3.4 \pm 0.3 \times 10^{22}$ cm^{-3} nominal conditions. Three to five frames out of the full eight frame dataset typically have sufficient S/N to infer conditions from the Mg lines. Each frame has orthogonal space and photon energy axes [Fig. 1(d)]. More details of the configuration and data processing are in [1–4,11]. Six FeMg experiments are included here, three of which had two UXI cameras. Plasma conditions were determined from a total of 33 frames (nine camera datasets).

Evaluating temporal gradients requires an accurate time-axis determination. We do this by fitting the time-resolved backlighter intensities with a Gaussian and defining the peak as $t = 0$ (see below). This time axis allows us to compare UXI data recorded from different experiments and to study the averages and reproducibility. First, we extract the spatial lineout centered at 8.22 ± 0.05 Å, where no Mg lines exist. Then, we average the intensity in ± 175 μm about the spatial peak. The high sensitivity of the UXI allows us to measure the backlighter intensity over 13 ns, which is more than 4 times longer than the backlighter FWHM. Because of the relatively coarse temporal resolution, we performed a Gaussian fit on each intensity profile versus time, with the Gaussian peak set to $t = 0$. The dataset cross-timing is such that the peak of the backlighter ($t = 0$) coincides in all datasets. The backlighter time history is measured on the six FeMg experiments and on calibration experiments that are identical except that the sample contained no FeMg layer embedded in the tamper. This provides a total of 303 data points for determining the backlighter time history and its uncertainty [Fig. 3(a), inset]. The total duration of the backlighter is 2.8 ± 0.15 ns after deconvolution of the gate integration time.

We determine the temperature and density using the methods described briefly above and thoroughly in [13]. The measured $T_e(t)$ rises with time [Fig. 2(a)]. The 1σ uncertainties (error bars) are dominated by the standard deviation over temperatures inferred from different line ratios. The weighted average over the nine datasets suggests the temporal shape of the temperature is linear. The temporal gradient corresponds to 10 eV/ns or a 160 to 210 eV rise over 5 ns. The measured n_e increases slightly over time, with 1.4×10^{21} cm^{-3}/ns, based on the linear fit to the weighted mean. However, the data are essentially constant within the uncertainties.

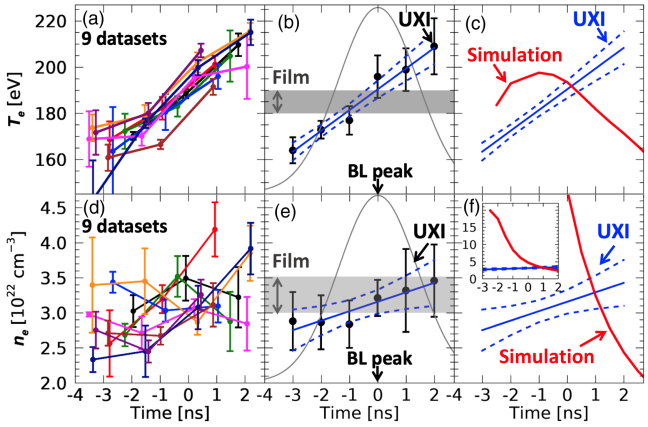

FIG. 2. (a) T_e evolution for anchor 2 Fe samples with uncertainties for nine camera datasets, with the number of measurements that overlap within 1-σ uncertainty matching the expected proportion [21]. (b) Weighted mean T_e and linear fit to weighted mean (blue; uncertainties are blue dash) overlaid with backlighter time history (black curve) and gray region corresponding to film results. (d),(e) n_e evolution over same datasets. Density measurements overlap within uncertainties, similar to the temperature. Trend shows a mostly constant density within measurement uncertainties. (c),(f) Comparison to past simulation results [3] with an inset for n_e (f) for full density variation in simulation.

Inferences from film-based measurements [9] intersect the UXI-based evolution at the backlighter peak [Figs. 2(b) and 2(e)]. The conditions inferred from the film-based recordings are a backlighter-weighted temporal average. Because of this weighting, the film measurements can be more accurately described as "*film-integrated*" rather than by the somewhat misleading "time-integrated" term.

Our past simulations do not agree with the observed temporal evolution, even though they agreed well with the backlighter-weighted average values [3]. The differences illustrate the experimental guidance for the simulation-based understanding. For example, since the density is already low several ns before the backlighter peak, x-ray preheat most likely causes the sample to expand. Our previous simulations could not be expected to reproduce this effect since the preheat presence was unknown. Furthermore, the simulated $T_e(t)$ and $n_e(t)$ decreased with time, and the charge state was roughly constant. However, the measured temperature increases, with density remaining roughly constant. Hence, ionization should increase with time. Refinement of these simulations using the new experimental data is a subject of future research.

Evaluating temporal gradient effects on film-integrated measurements—The plasma condition changes reinforce the need to determine the temporal gradient effects on the film-integrated results. The test here uses measured time-resolved conditions, backlighter time history, and modeled opacity predictions. The spectrum obtained is thus called synthetic *film-integrated* spectrum. It is only synthetic because we used modeled opacities, but all other quantities are measured. The synthetic film-integrated spectrum is used to evaluate the importance of temporal gradients, assuming the modeled opacities are correct. At each time, the models predict absorption spectra at the measured $T_e(t)$, $n_e(t)$, and backlighter intensity values. The sequential absorption spectra are summed, and the results are analyzed as if the spectra were film-integrated data. Comparison with a "single point" [i.e., single-(T_e, n_e)] opacity model calculation at the backlighter-averaged T_e and n_e quantifies the importance of temporal gradients.

First, the film-integrated attenuated and unattenuated FeMg backlighter spectra are simulated from the measured $T_e(t)$, $n_e(t)$, and time-resolved backlighter. Five temporal points t_i, with i = 1 to 5, are selected over the central 5 ns of the backlighter [Fig. 3(a), inset]. The backlighter spectrum at each time point is assumed Planckian with a color temperature such that the relative backlighter time history matches the Planckian function at 8.22 Å wavelength and for a temperature at a peak time of 370 eV [4]. The time-resolved FeMg transmission spectra are computed with PrismSPECT [12] at those times for the inferred

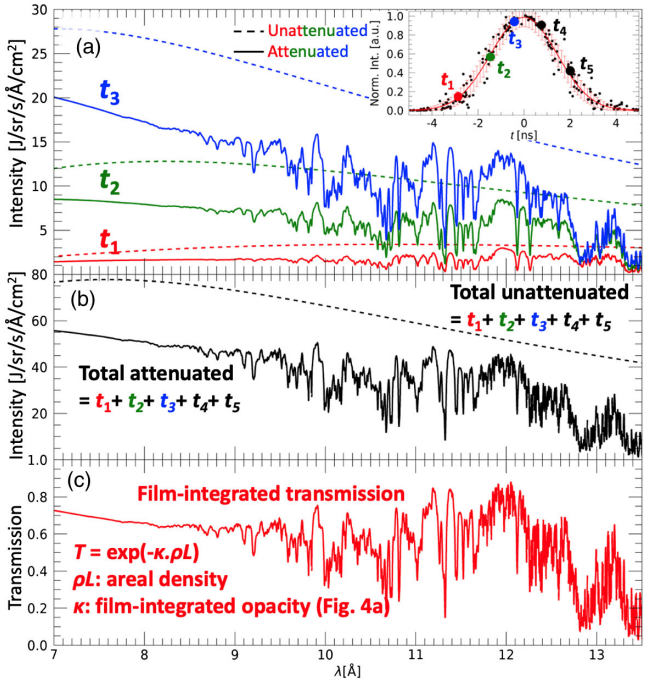

FIG. 3. (a) Unattenuated (dashed) and attenuated (solid) spectra using calculated opacities [12] for five time steps, with only the first three shown for legibility, all times shown in Appendix in Fig. 5. The five time steps total corresponds to the duration of measured (T_e, n_e) and encompasses most of the backlighter time history (inset, measurements from 303 temporal points normalized to peak of Gaussian fit on each dataset, with times labeled for gradient study). (b) Total unattenuated or attenuated (dashed and solid) for all five timesteps. (c) Ratio of total attenuated to total unattenuated to form synthetic *film-integrated* transmission.

$T_e(t)$ and $n_e(t)$ [Figs. 2(b) and 2(e)] and typical Mg and Fe areal densities (i.e., 2.5×10^{18} Mg/cm^2 and 2×10^{18} Fe/cm^2). Then, each transmission spectrum is multiplied by the time-resolved backlighter at each t_i to simulate the time-resolved FeMg attenuated spectrum [Fig. 3(a)]. After applying instrumental spectral broadening, the spectra are summed over all t_i to simulate the FeMg synthetic film-integrated attenuated and unattenuated backlighter spectra [Fig. 3(b)].

Next, Fe opacity spectra are inferred from the synthetic film data shown in Fig. 3(b). The attenuated spectra (solid) are divided by the unattenuated spectra (dashed) to infer the synthetic film-integrated FeMg transmission spectra [Fig. 3(c)]. Mg lines are analyzed to infer the film-equivalent T_e and n_e, which were 189.6 eV and 3.13×10^{22} cm^{-3}. The Mg transmission is removed from Fig. 3(c) by dividing it by the Mg transmission computed at the inferred conditions. Then, the Fe-only film-integrated transmission is converted to opacity by evaluating $\kappa_\lambda = -\ln T_\lambda/\rho L$, where ρL is the Fe areal mass density, to obtain synthetic film-integrated spectra for comparison with single-point models.

Figure 4(a) shows the synthetic film-integrated opacity (red), and the Fe opacity calculated at film-inferred single-point conditions (blue). The difference between the two [Fig. 4(b), green] is smaller than the difference between the published Z data and the experimentally equivalent opacity [Fig. 4(b), black] by 2 to 3 times the uncertainty of the Z data. Thus, temporal integration of the film-integrated data for the published spectral range does not explain the model-data discrepancy.

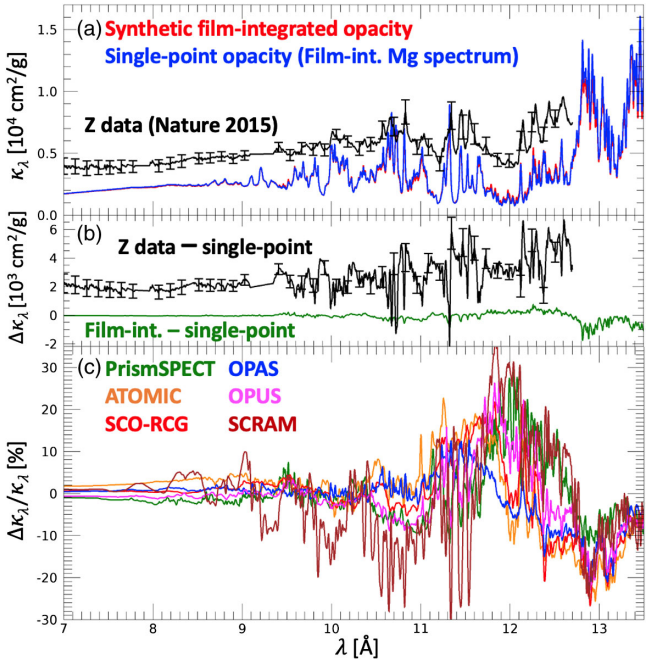

FIG. 4. (a) Comparison of synthetic film-integrated opacity and single-point opacity calculated at film-inferred conditions $\kappa_\lambda^{\text{model}}(T_e^{\text{film}}, n_e^{\text{film}})$ and published opacity [1]. (b) Difference of synthetic film-integrated and single-point opacities (green) compared with difference of Z data and single-point opacity (black). Predicted film-integration effect is well below and outside Z data uncertainties. (c) Relative difference of synthetic film-integrated to single-point opacities for leading opacity models.

An assumption of the foregoing conclusion is that the opacity models are correct. To assess the effect of a specific opacity model, based on its own approximations, we performed a series of calculations for the ATOMIC [22], SCO-RCG [23], OPAS [24], OPUS [25], and SCRAM [26] opacity models. The impact of the time-integration effects is summarized in Fig. 4(c). The conclusion is similar for all of the models, with a predicted gradient effect several times lower than the measurement uncertainties.

Our new measurements use a novel technology to measure opacity sample evolution on Z. These measurements quantify the impact of temporal gradients on published film-integrated data and contradict the hypothesis that the temporal evolution might explain the published model-data discrepancy. The ultimate approach to resolving the model-data discrepancy entails measuring Fe opacity as a function of time. However, that must satisfy many more requirements, including absolute transmission measurements, rather than line optical depth reported here, and formal uncertainty determination, while measuring plasma conditions. Such an absolute opacity approach is presently under investigation.

Accurate time-resolved absolute opacity measurements with verified uncertainties would provide measurements at multiple conditions in a single Z experiment. Suppressing preheat would enable measurements at higher density, since the sample is initially solid. Reducing preheat could delay the expansion with respect to the backlighter pulse. Deploying a next generation Daedalus hCMOS sensor [17] with a ~1 ns gate time would correspond to about 2 times the temporal resolution and 3 times the dynamic range for higher sensitivity. This would be especially useful where the density evolves rapidly in a nonlinear way. Accessing these new conditions could provide more opportunities to compare with other opacity platforms such as Opacity-on-NIF [27]. Furthermore, the time-resolved UXI is being deployed in future Opacity-on-NIF experiments due to the unique camera advantages.

Acknowledgments—We thank the entire Z facility team, and L. Claus and M. Sanchez for UXI development support at the Sandia MESA facility. We thank B. Adams, A. Stephens, and L. Swiler for support with the Sandia Dakota code. We thank T. A. Gomez for providing detailed line shape calculations used in the line fitting algorithm. Sandia National Laboratories is a multimission laboratory managed and operated by National Technology and

Engineering Solutions of Sandia, LLC, a wholly owned subsidiary of Honeywell International Inc., for the U.S. Department of Energy's National Nuclear Security Administration under Contract DE-NA0003525. Los Alamos National Laboratory is operated by Triad National Security, LLC, for the National Nuclear Security Administration of the U.S. Department of Energy (Contract No. 89233218CNA000001).

This Letter describes objective technical results and analysis. Any subjective views or opinions that might be expressed in the Letter do not necessarily represent the views of the U.S. Department of Energy or the United States Government.

[1] J. E. Bailey *et al.*, Nature (London) **517**, 56 (2015).
[2] T. Nagayama *et al.*, Phys. Rev. Lett. **122**, 235001 (2019).
[3] T. Nagayama, J. E. Bailey, G. Loisel, G. A. Rochau, J. J. MacFarlane, and I. Golovkin, Phys. Rev. E **93**, 023202 (2016).
[4] T. Nagayama, J. E. Bailey, G. P. Loisel, G. A. Rochau, J. J. MacFarlane, and I. E. Golovkin, Phys. Rev. E **95**, 063206 (2017).
[5] R. M. More, S. B. Hansen, and T. Nagayama, High Energy Density Phys. **24**, 44 (2017).
[6] M. K. G. Kruse and C. A. Iglesias, High Energy Density Phys. **31**, 38 (2019).
[7] J. E. Bailey, G. A. Rochau, R. C. Mancini, C. A. Iglesias, J. J. MacFarlane, I. E. Golovkin, J.-C. Pain, F. Gilleron, C. Blancard, P. Cossé, G. Faussurier, G. A. Chandler, T. J. Nash, D. S. Nielsen, and P. W. Lake, Rev. Sci. Instrum. **79**, 113104 (2008).
[8] B. M. Adams, W. J. Bohnhoff, K. R. Dalbey, M. S. Ebeida, J. P. Eddy, M. S. Eldred, R. W. Hooper, P. D. Hough, K. T. Hu, J. D. Jakeman, M. Khalil, K. A. Maupin, J. A. Monschke, E. M. Ridgway, A. A. Rushdi, D. T. Seidl, J. A. Stephens, L. P. Swiler, and J. G. Winokur, Dakota, A multilevel parallel object-oriented framework for design optimization, parameter estimation, uncertainty quantification, and sensitivity analysis: Version 6.14 user's manual, Sandia National Laboratories SAND2021-5822, 2021.
[9] T. Nagayama, J. E. Bailey, D. C. Mayes, G. P. Loisel, and G. S. Dunham, Sequential spectral line analysis for accurate density and temperature diagnosis of laboratory opacity measurements (to be published).
[10] T. A. Gomez, T. Nagayama, P. B. Cho, M. C. Zammit, C. J. Fontes, D. P. Kilcrease, I. Bray, I. Hubeny, B. H. Dunlap, M. H. Montgomery, and D. E. Winget, Phys. Rev. Lett. **127**, 235001 (2021).
[11] G. Dunham, T. Nagayama, J. Bailey, and G. Loisel, Rev. Sci. Instrum. **92**, 08351 (2021).
[12] J. J. MacFarlane, I. E. Golovkin, P. Wang, P. R. Woodruff, and N. A. Pereira, High Energy Density Phys. **3**, 181 (2007).
[13] T. Nagayama *et al.*, High Energy Density Phys. **20**, 17 (2016).
[14] M. R. Gomez, G. A. Rochau, J. E. Bailey, G. S. Dunham, M. D. Kernaghan, P. Gard, G. K. Robertson, A. C. Owen, J. W. Argo, D. S. Nielsen, and P. W. Lake, Rev. Sci. Instrum. **83**, 10D714 (2012).
[15] J. L. Porter, Q. Looker, and L. Claus, Rev. Sci. Instrum. **94**, 061101 (2023).
[16] Q. Looker, A. P. Colombo, M. Kimmel, and J. Porter, Rev. Sci. Instrum. **91**, 043502 (2020).
[17] Q. Looker, M. Kimmel, C. Yang, and J. L. Porter, Rev. Sci. Instrum. **94**, 113505 (2023).
[18] L. Claus, L. Fang, R. Kay, M. Kimmel, J. Long, G. Robertson, M. Sanchez, J. Stahoviak, D. Trotter, and J. L. Porter, Target Diagnostics Physics and Engineering for Inertial Confinement Fusion IV, *International Society for Optics and Photonics 9591* (SPIE Digital Library, Bellingham, WA, 2015), 95910P, 10.1117/12.2188336.
[19] L. Claus, T. England, L. Fang, G. Robertson, M. Sanchez, D. Trotter, A. Carpenter, M. Dayton, P. Patel, and J. L. Porter, in *Proceedings of the SPIE, Target Diagnostics Physics and Engineering for Inertial Confinement Fusion VI 10390* (SPIE Digital Library, Bellingham, WA, 2017), 103900A, 10.1117/12.2275293.
[20] G. A. Rochau, J. E. Bailey, Y. Maron, G. A. Chandler, G. S. Dunham, D. V. Fisher, V. I. Fisher, R. J. Lemke, J. J. MacFarlane, K. J. Peterson, D. G. Schroen, S. A. Slutz, and E. Stambulchik, Phys. Rev. Lett. **100**, 125004 (2008).
[21] P. R. Bevington and D. K. Robinson, *Data Reduction and Error Analysis for the Physical Sciences* (McGraw-Hill, New York 2003).
[22] J. Colgan, D. P. Kilcrease, N. H. Magee, M. E. Sherrill, J. J. Abdallah, P. Hakel, C. J. Fontes, J. A. Guzik, and K. A. Mussack, Astrophys. J. **817**, 116 (2016).
[23] J.-C. Pain and F. Gilleron, High Energy Density Phys. **15**, 30 (2015).
[24] C. Blancard, P. Cossé, and G. Faussurier, Astrophys. J. **745**, 10 (2012).
[25] D. Aberg, D. Fenn, M. E. Foord, P. E. Grabowski, C. A. Iglesias, and B. G. Wilson, The OPUS radiative opacity code, a new implementation of the upper-transition array method, Lawrence Livermore National Laboratory LLNL-TR-813832, 2020.
[26] S. B. Hansen, J. Bauche, C. Bauche-Arnoult, and M. F. Gu, High Energy Density Phys. **3**, 109 (2007).
[27] T. S. Perry, R. F. Heeter, Y. P. Opachich, H. M. Johns, J. A. King, E. S. Dodd, B. G. DeVolder, M. E. Sherrill, B. G. Wilson, C. A. Iglesias, J. L. Kline, K. A. Flippo, T. Cardenas, M. B. Schneider, D. A. Liedahl, T. J. Urbatsch, M. R. Douglas, J. E. Bailey, and G. A. Rochau, High Energy Density Phys. **35**, 100728 (2020).

End Matter

Appendix—In the main article, having all five time steps in the same plot of Fig. 3(a) created a nonlegible plot due to overlapping curves. Here, all t_1 through t_5 time steps are shown in separate plots.

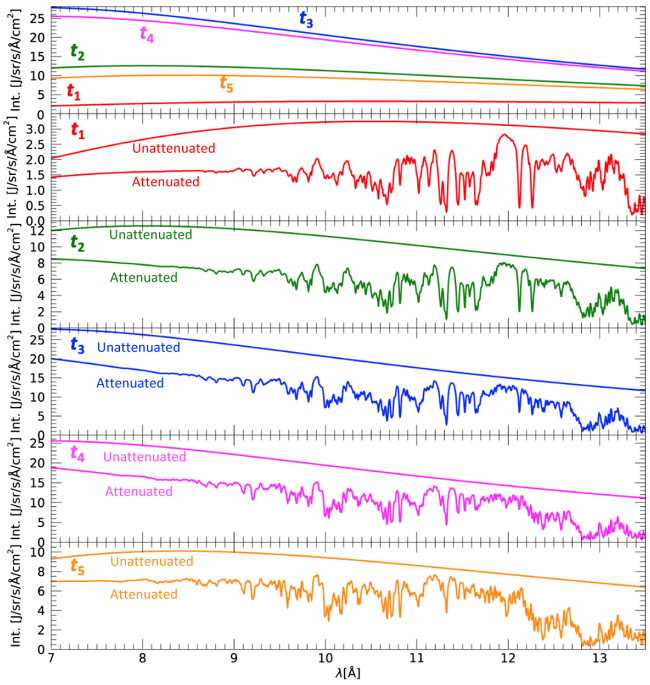

FIG. 5. Top: All unattenuated spectra at time steps [dashed curved in main article Fig. 3(a)]. Plots below: for each t_i, i = 1 to 5, unattenuated and attenuated using calculated opacities [12] for five time steps. The five time steps total corresponds to the duration of measured (T_e, n_e) and encompasses most of the backlighter time history.